Cost-Effective Prognostics of IGBT Bond Wires With Consideration of Temperature Swing

Keting Hu, *Student Member, IEEE*, Zhigang Liu, *Senior Member, IEEE*, He Du, *Student Member, IEEE*, Lorenzo Ceccarelli, *Student Member, IEEE*, Francesco Iannuzzo, *Senior Member, IEEE*, Frede Blaabjerg, *Fellow, IEEE*, and Ibrahim Adamu Tasiu, *Student Member, IEEE*

***Abstract*—This article presents a cost-effective prognostic method for the bond wires in the insulated-gate bipolar transistor (IGBT). Consider that the crack propagation in the wire bond leads to the bond wire liftoff, the corresponding state equation is established from the fracture mechanics theory, with the consideration of the uneven distribution of the temperature swings. Hence, the proposed model can work under different loading conditions. With the fact that the ON-state voltage ($v_{\mathrm{ce,on}}$) of the IGBT shifts with the crack propagation, the history $v_{\mathrm{ce,on}}$ is used to predict the remaining useful lifetime (RUL), through which numerous power cycling tests are avoided, and low economical cost for doing prognosis is fulfilled. In this article, the functional relationship between the increase of $v_{\mathrm{ce,on}}$ and the crack length of each bond wire is obtained through finite-element simulation, while the effects of the temperature variation and metallization degradation to the $v_{\mathrm{ce,on}}$ are compensated. Thus, the output equation can be obtained. Then, the unknown parameters of the aforementioned equations and the current crack length can be estimated by the particle-based marginalized resample-move algorithm. Finally, the RUL can be predicted effectively by evolving the particles obtained in the algorithm. The proposed method has been validated by the power cycling test.**

***Index Terms*—Bond wire lifetime, crack propagation, finite element, insulated-gate bipolar transistor (IGBT), marginalized resample move.**

I. Introduction

INSULATED-GATE bipolar transistor (IGBT)-based power converters are widely utilized in modern industry, including wind turbines [1], electrified vehicles [2]–[4], high-current dc electric power transmission systems [5], [6], etc. Though the power converter shows the great success in the industry, several papers have pointed out that the power converters take a significant part in the system failures, in which the power electronics component is one of the primary failure roots [7]–[9]. As a consequence, the reliability of power converters and especially the reliability of power electronics components have drawn considerable attention in recent years for the sake of safety and economy [10]–[13].

Package-related failure is one of the most common failures in IGBT modules, which is caused by the coefficients of thermal expansion (CTE) mismatch between different stacks inside the component [14]. When the IGBT is operating, periodical power losses are produced, and temperature swings are caused within the power module. Combined with the CTE mismatch, significant thermo-mechanical stresses are introduced to the joints between different stacks. Notably, the wire bonds and die-attach solder joints suffer higher stresses because of a more significant CTE mismatch. As a result, the bond wire degradation and solder fatigue are the two dominant wear-out failures in practice [15]. It should be pointed out that the former will be the focus of this article, though both of them could degrade the performance of the IGBT module as time goes by, and destroy the component in the end, if no proper measures were taken.

Condition monitoring (CM) and prognostics are two fundamental approaches to improve the reliability of the IGBTs [12]. The CM focuses on monitoring the damage sensitive parameters online to get an insight into the current health state of the IGBT. Once the unhealthy states or incipient faults have been detected, further actions will be implemented to avoid catastrophic consequences. On the other hand, the prognostics are capable of giving how much time the component can keep running functionally in the future, subjecting to specific loads. Consequently, the risk of failure could be minimized while the component is in service [16].

Usually, the CM is the basis because it is impossible to perform the prognostics without any information about the component. The ON-state voltage ($v_{\mathrm{ce,on}}$) of the IGBT is the most chosen precursor, based on which numerous prognostic methods have been studied.

Generally, the prognostic methods can be classified into two categories, i.e., model-driven approach and data-driven approach. For the model-driven techniques, there are three main steps to predict the remaining useful lifetime (RUL) [17]–[20]. First of all, the mission profile of power converters should be translated into the junction temperature. With the help of the corresponding control strategy, wind speed, solar irradiance, or the driving speed will be converted to the input current and input voltage of operating converters. Then, the junction

Manuscript received August 9, 2019; revised October 25, 2019; accepted December 12, 2019. Date of publication December 12, 2019; date of current version March 13, 2020. This work was supported by the Natural Science Foundation of China under Grant U1434203 and Grant U1734202. Recommended for publication by Associate Editor A. Lindemann. *(Corresponding author: Keting Hu.)*

K. Hu, Z. Liu, and I. A. Tasiu are with the School of Electrical Engineering, Southwest Jiaotong University, Chengdu 611756, China (e-mail: huketing121@163.com; liuzg_cd@126.com; ibrele@yahoo.com).

H. Du, L. Ceccarelli, F. Iannuzzo, and F. Blaabjerg are with the Department of Energy Technology, Aalborg University, Aalborg 9220, Denmark (e-mail: hdu@et.aau.dk; lce@et.aau.dk; fia@et.aau.dk; fbl@et.aau.dk).

Color versions of one or more of the figures in this article are available online at http://ieeexplore.ieee.org.

Digital Object Identifier 10.1109/TPEL.2019.2959953

temperature of each IGBT can be obtained through the electrothermal simulation or by the calculation of power loss and thermal impedance. Second, the temperature should be transferred to damage information on the component through an empirical lifetime model. The Coffin–Manson equation is a widely adopted model to describe the link between the junction temperature swing and the lifetime of the IGBT. Later, the mean junction temperature, cycle frequency, power-ON time, blocking voltage, current per bond wire, and the bond wire diameter are included in the lifetime model to get a more accurate characterization of the lifetime [21]–[24]. Finally, the accumulated damage of the corresponding mission profile can be computed based on the Miner's rule, and the RUL can be inferred as how many times the IGBT module could operate under this mission profile. However, it should be pointed out that with the degradation of the IGBT module, the junction temperature will rise under the same mission profile, because $v_{\mathrm{ce,on}}$ increases and the heat dissipation path is reduced. Feedback from the damage accumulation to the electrothermal simulation will be required to avoid over-optimistic results [17].

The data-driven methods mainly focus on the $v_{\mathrm{ce,on}}$ data to extract the RUL information. Nevertheless, it is not easy to acquire enough data from the practical application in a short time, because the lifetime of the power module could be several years and even tens of years. To address this problem, the accelerated power cycling test could be a solution for validation [21], [25], [26]. By operating the power modules under high thermal stress, the components would degrade much faster than under normal operating conditions. Thus, the data collection can be finished within a few weeks and even several days. The most straightforward data-driven method is to predict the RUL by training. In [16], the $v_{\mathrm{ce,on}}$ data are discretized into several phases depending on the IGBT health states. After the noise is filtered by a low-pass filter, the duration of each phase, together with the corresponding RUL are fed to a neural network (NN) and the adaptive neuro-fuzzy inference system (ANFIS) for training. The results show that NN outperforms ANFIS in the case of [16]. As an improved method, a stochastic process is combined with a time-delay neural network to predict the RUL, which can provide a confidence interval [27]. The uncertainty is also considered in [28]. It models the discrete degradation process by various probability distributions. Then, Monte Carlo simulations are carried out to estimate the precursor value up to the failure criterion. To enhance the prognostic ability for varying load conditions, the precursors could be unified before fed to the ANFIS [29].

Unfortunately, the performance of the aforementioned data-driven method is not so satisfying due to the small dataset scale. In spite of accelerated tests, it is still a problem to collect enough data in a short time. An alternative solution could be to utilize the history information. In [30], the available precursor data are collected to do curve fitting at some point of the lifetime, based on the knowledge of the failure process. Thus, the RUL can be fulfilled by extrapolating the precursor. The results indicate that the later the prediction is performed, the better the accuracy will be. A more sophisticated version of this method is to replace the extrapolation with the particle filter (PF), which can deal with the uncertainty. In [31] and [32], the sequential importance resampling PF and auxiliary PF (APF) are utilized to predict the RUL, respectively. It turns out that the APF has higher prediction accuracy and narrower probability density function. It should also be noted that the Mahalanobis distance between $v_{\mathrm{ce,on}}$ and collector–emitter current (I_{ce}) is calculated to determine the anomaly and trigger the prediction in [31].

Though the aforementioned methods can achieve their successes in predicting the RUL, there are still challenges. For the model-driven approach, it requires numerous power cycling tests to find out the parameters of the empirical model, which is time consuming and uneconomical. This problem could be more severe when more and more parameters are taken into the model. Meanwhile, the mission profile selection also requires further investigations. For the training methods of the data-driven approach, as mentioned earlier, the performance under small-scale data should be improved. As for the history data-based methods, most of them hold the assumption that the load is constant, i.e., the temperature keeps steady throughout the whole lifetime. If the load is not constant, the fitted model may be different from the real one and leads to an unreliable result.

The contribution of this article is given as follows.

1) This article proposes a fusion method of the model-driven and data-driven approach, which inherits the advantages of both approaches to attain the cost efficiency and the capability of dealing with the temperature swing variation (TSV) condition at the same time.
2) The system model is established from the physics-of-failure view with the aid of finite-element simulation, rather than by a simple curve fitting.
3) An accurate finite-element model of the IGBT module is presented.
4) The features derived from the finite-element analysis make it possible to describe the crack propagation processes of all the wire bonds simultaneously.
5) The temperature and metallization reconstruction effects on the $v_{\mathrm{ce,on}}$ are compensated.

The rest of this article is organized as follows. Section II contains the finite-element simulation results. The system modeling with the temperature and metallization reconstruction consideration will be given in Section III. The lifetime prediction scheme is described in Section IV. Section V presents the experimental results, and finally, Section VI concludes this article.

II. Finite-Element Simulation

To establish the physics-of-failure model of the bond wire degradation process, the bond temperature is required to be known. Though the IR camera can measure the surface temperature of an open module, it is not applicable to measure the temperature of the bonds that are shielded by the bond wires. Besides, it is also not possible to link the temperature, bond crack length, and the increase of $v_{\mathrm{ce,on}}$ together during the power cycling test. Given this circumstance, finite-element simulations are carried out in COMSOL to tackle the aforementioned problems.

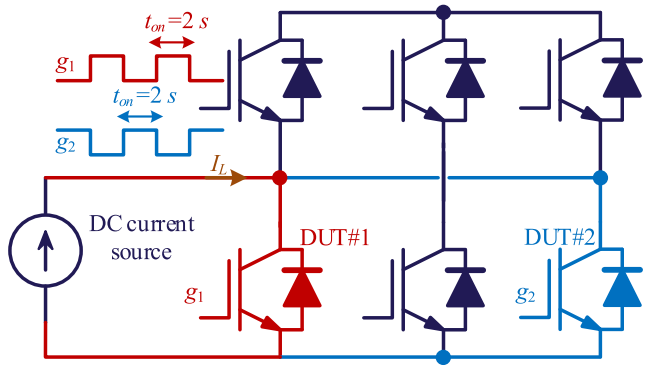

Fig. 1. Power cycling test configuration using a six-pack IGBT module.

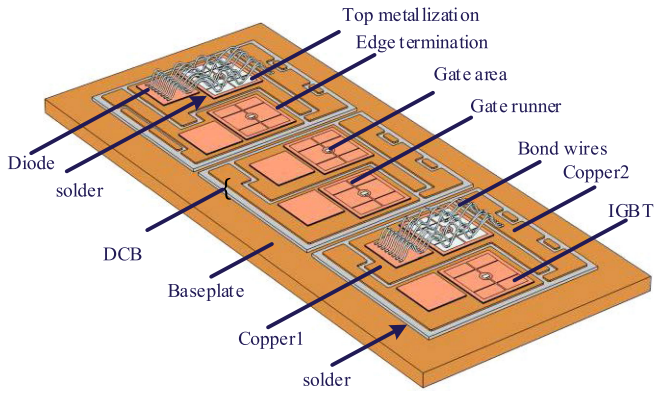

Fig. 2. Geometry of the finite-element model of the six-pack IGBT module.

A. Geometry

The configuration of the target power module can be seen in Fig. 1 and the geometrical model of the IGBT module is given in Fig. 2. To comply with the accelerated power cycling test condition, only the lateral IGBTs on the low side are stressed and analyzed in detail. The rest of IGBTs and all the diodes are simplified by removing the top metallization and bond wires without significant errors on the results. For each IGBT, the gate area is in the center of the IGBT, the gate runner separates the active areas, and the termination is located at the edge. All of them do not carry the load current when the IGBT is conducting, which results in the uneven temperature distribution of the die. Besides, two solder layers are considered in the model. One is between the die and the direct copper bonded (DCB) substrate, while another lies between the DCB and the baseplate. Table I shows the geometry sizes of all the layers as mentioned previously.

B. Material Property and Boundary Condition

As it is well-known that the material properties, i.e., thermal and electrical nature, are temperature dependent, the temperature characterizations of the materials are taken into account in the finite-element model. For the electrical parameters, the electrical conductivity governed by the temperature is considered. Linear approximation of the resistivity is adopted for the electrical

TABLE I
GEOMETRIC SIZE OF THE FINITE-ELEMENT MODEL

Layer	Material	Thickness (um)	Dimensions (mm×mm)
Bond wire	Aluminum	ϕ375	none
Metallization	Aluminum	3.2	complied
IGBT	Silicon	115	11.31×12.56
Diode	Silicon	115	8.15×9
Die solder	SAC305	135	complied
	Copper	300	34.53×30.69
DCB	Al_2O_3	600	37.125×33
	Copper	300	34.53×30.69
Baseplate solder	SAC305	200	complied
Baseplate	copper	3000	50×115

conductivities of the aluminum and the copper, as shown in the following:

$$\frac{1}{\sigma(T)} = \frac{1}{\sigma_0}\left[1 + \beta(T - T_0)\right] \tag{1}$$

where σ represents the electrical conductivity at temperature T, σ_0 the electrical conductivity at the reference temperature, β the temperature coefficient, and T_0 the reference temperature. According to [33], $\sigma_0 = 3.77 \times 10^7$ S/m and $\beta = 0.00404\ \mathrm{K}^{-1}$ for the aluminum, and $\sigma_0 = 5.95 \times 10^7$ S/m and $\beta = 0.00390\ \mathrm{K}^{-1}$ for the copper, with the reference temperature at 20 °C.

However, the electrical conductivity of the die active area will be realized in another way. Since the electrical conductivity not only depends on the temperature but also on the current flowing through it (or the voltage across it during conducting), the electrical conductivity at different current and temperature could be obtained through the datasheet. It should be pointed out that the curve tracer may not be applicable here because it measures the terminal-to-terminal voltage, instead of the voltage across the die. When applying the temperature- and current-/voltage- dependent σ_{die} in the COMSOL, the main problem is that the current cannot be measured directly and the voltage is not distributed evenly inside the die. This problem could be settled by introducing the electric field strength in the vertical axis, which is the quotient of voltage and distance. Thus, the interpolated σ_{die} that is related to the temperature and electric field strength can be used in the finite-element simulation, as shown in Fig. 3.

On the other hand, two thermal properties are included in the simulation, namely, the thermal conductivity (k), and the specific heat capacity (Cp), both of which depend on the temperature. Their values at different temperatures are as shown in Table II [33], [34].

The boundary conditions are set in line with the testing condition, i.e., the current source with 125 A is set at Copper1, while Copper2 is set as the ground (see Fig. 2). Accordingly, the heat is generated in the dies and the bond wires at the same time, and alternately in DUT#1 and DUT#2. Meanwhile, the heat transfer coefficient is set to 875 W/m^2·K at the bottom of the baseplate to emulate the cooling plate and set to 50 W/m^2·K on the other surfaces to represent the natural cooling. The ambient

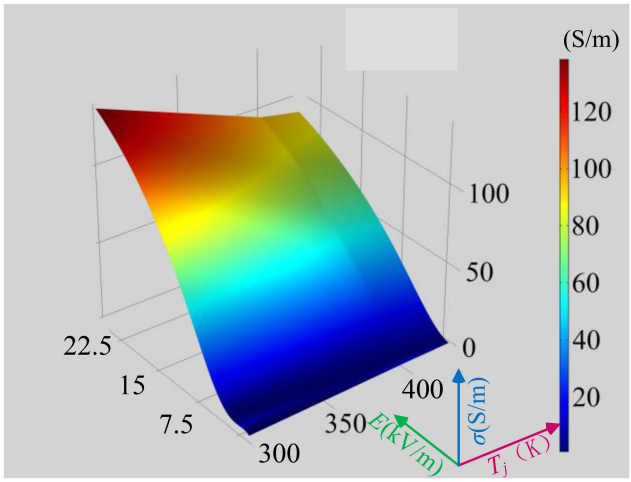

Fig. 3. Electrical conductivity of the die related to the temperature and electric field strength inside the die.

TABLE II
THERMAL PROPERTIES OF THE MATERIALS [33], [34]

Material	Property	Temperature (°C)		
		25	125	225
Aluminum	k (W/m·K)	237	240	236
	Cp (J/kg·K)	897	955.5	994.8
Silicon	k (W/m·K)	148	98.9	76.2
	Cp (J/kg·K)	705	788.3	830.7
SAC305	k (W/m·K)	57	57	57
	Cp (J/kg·K)	220	220	220
Copper	k (W/m·K)	401	393	386
	Cp (J/kg·K)	385	398.6	407.7
Al_2O_3	k (W/m·K)	37	27.2	20.9
	Cp (J/kg·K)	785.5	942	1076

temperature is set at 35 °C with the consideration that it will rise due to the heat dissipated by the module. Note that the boundary condition should be reset accordingly when the module operates in other applications.

C. Simulation Results

As mentioned previously, only the maximum and minimum temperatures are recorded during the power cycling test, and a verification test is performed for the finite-element simulation. It records the temperature continuously with a sampling frequency at 1 kHz when the module reaches the thermal equilibrium. Meanwhile, the simulated temperature is exported as well at the same sensing point [sensing point 1 in Fig. 4(a)]. Therefore, the uneven temperature distribution effects are negligible in this case. A comparison between the tests and the simulations is given in Fig. 4(b). It can be seen that the simulation matches well with the test, which shows the effectiveness of the finite-element model.

Fig. 4(a) depicts the simulated temperature distribution of the IGBT module. It can be concluded that the temperatures

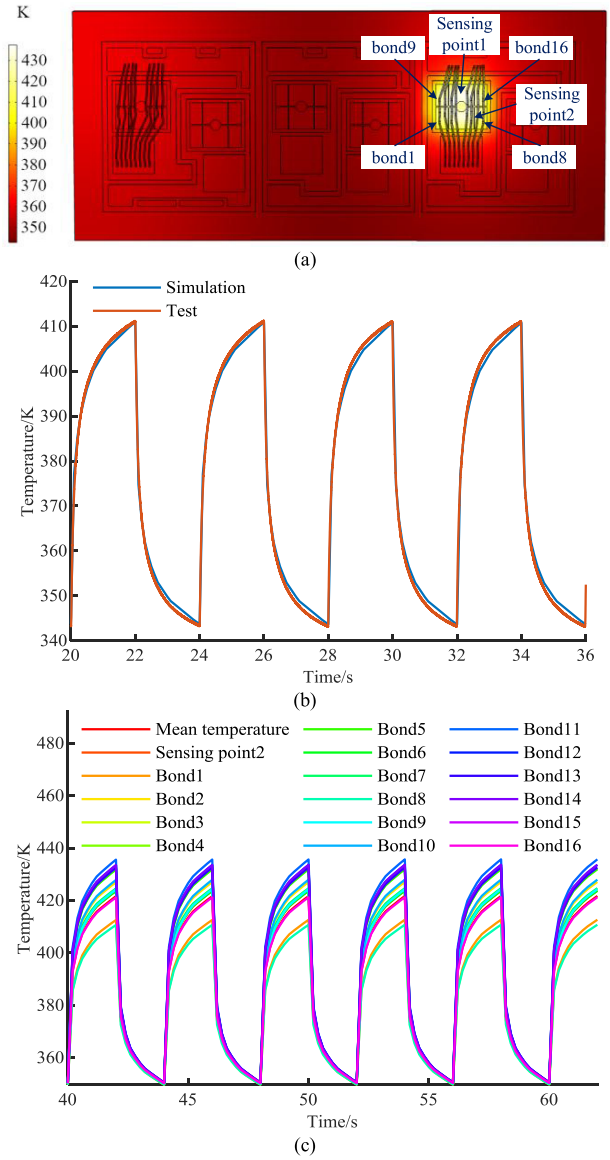

Fig. 4. Finite-element simulation results. (a) Temperature distribution of the module when the DUT#1 reaches the maximum temperature. (b) Comparison between the simulation result and the test result. (c) Simulation results of the temperatures of different parts inside the component.

of different areas of the module are significantly different. The highest temperature point appears on the bond wire, and the temperature of the inner part of the active area is higher than the others. When comparing the temperatures of all the bonds, bond 11 is the hottest. The temperatures of different parts inside the component are given in Fig. 4(c), including all the bonds, the sensing point 2 and the average value of the active area of the die. The parameters mentioned previously will be used to model the bond degradation process in Section III.

III. STATE-SPACE MODEL OF THE DEGRADATION PROCESS

Primarily, the bond wire liftoff is caused by the thermomechanical stresses that initiate and propagate the cracks in the aluminum wire near the bond, from both edges. It is a typical

fracture mechanics problem that has been studied since the last century. The process can be classified into three stages, namely, initiation, propagation, and unstable region. Usually, the first stage consumes most of the lifetime to form the initial crack, with the help of cyclic stresses and the defects in the specimens. In the case of wire bonding, however, the situation may differ. According to [35]–[37], the ultrasonically wire bonding could damage the bonds and make them vulnerable, even precrack could have been the result. As a consequence, the lifetime of the bond wire could be regarded roughly as the time that propagating to the critical crack length needs. This assumption is the basis of the prognostic method in this article.

A. State Equation

Consider the fact that the absolute junction temperature contributes much more to the solder fatigue than to the bond wire fatigue, the Paris' equation is selected here to describe the crack propagation as shown in the following equation [38], [39]:

$$\frac{da}{dN} = C(\Delta k)^m \tag{2}$$

where a represents the crack length of one side for a double edge notch specimen, N is the cycles, Δk is the stress intensity factor, and C and m are the constants.

Basically, Δk is influenced by the cyclic stress $\Delta\sigma$, the geometry factor Y, and the crack length a, which can be described as

$$\Delta k = \Delta\sigma \cdot Y \cdot \sqrt{\pi \cdot a}. \tag{3}$$

$\Delta\sigma$ is caused by the combination of the temperature difference and the CTE mismatch, which can be obtained through the stress–strain curve, as shown in Fig. 5(a) [40]. The strain is calculated as

$$\Delta\varepsilon = \Delta\alpha \cdot \Delta T \tag{4}$$

where $\Delta\alpha$ indicates the CTE difference between the aluminum and the silicon. Fig. 5(b) gives the stress–strain curve around the working point of the IGBT module, which will be used later to simulate the crack propagation.

The parameter Y depends on the geometry information of the specimen. According to [41], it could be described in (5) shown at bottom of this page, where b is half of the length of the specimen. Mohsin [42] pointed out, nevertheless, that the crack location information, i.e., the ratio between the crack length a, and the specimen height $2h$, as well as the ratio between the crack length and the specimen length, also influences Y, which will of course have an impact on the crack propagation rate. For the conciseness of this article, the correctness factor is given directly here as 7.54, which is derived from the results in [42]. The parameters are given as $2h = 280$ μm, $2b = 800$ μm, and shown in Fig. 6.

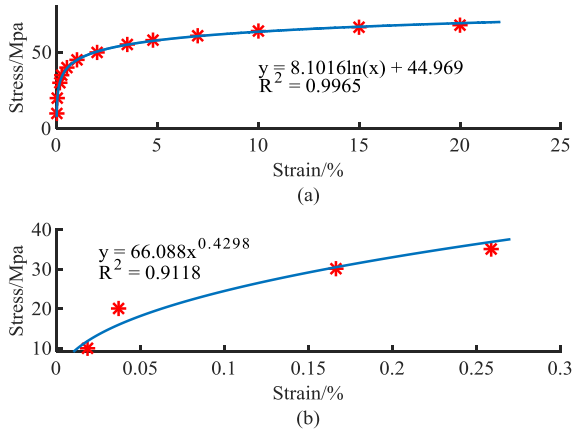

Fig. 5. Stress–strain curve of the aluminum bond wire (a) for the whole range and (b) around working point [41].

Combining (2)–(5), the state equation of the crack propagation can be described in (6) shown at bottom of this page, where σ_1 is the process noise, and m is given as 3.2, according to [43].

B. Output Equation

The cracks in the bonds increase the resistance of the IGBT. As a consequence, $v_{\mathrm{ce,on}}$ keeps rising during the aging, and it can be utilized as a precursor for the RUL. In reality, besides the bond wire degradation, $v_{\mathrm{ce,on}}$ is affected by the other two factors, namely, temperature, and metallization degradation (solder fatigue can be regarded as temperature). Thus, it is important to consider these two when modeling the $v_{\mathrm{ce,on}}$-based output equation.

1) Temperature: The value of $v_{\mathrm{ce,on}}$ varies with the temperature significantly though the current keeps constant, as demonstrated in Fig. 3. As a result, the temperature component of $v_{\mathrm{ce,on}}$ must be eliminated before the RUL prediction. Two mechanisms increase and decrease the voltage with the increasing temperature at the same time. When the current is low, $v_{\mathrm{ce,on}}$ decreases with the temperature and the opposite for the high current. But for the same current, the temperature coefficient is

$$Y = \sqrt{\pi \cdot a} \times \frac{1.122 - 0.56\,(a/b) - 0.205(a/b)^2 + 0.471(a/b)^3 - 0.190(a/b)^4}{\sqrt{1 - a/b}} \tag{5}$$

$$\frac{da}{dN} = C\left[(8.1016 \times (\ln(\Delta\alpha \cdot \Delta T \times 100\%) + 44.969)) \cdot \sqrt{\pi \cdot a} \times 7.54 \times \frac{1.122 - 0.56\,(a/b) - 0.205(a/b)^2 + 0.471(a/b)^3 - 0.190(a/b)^4}{\sqrt{1 - a/b}}\right]^{3.2} + \sigma_1 \tag{6}$$

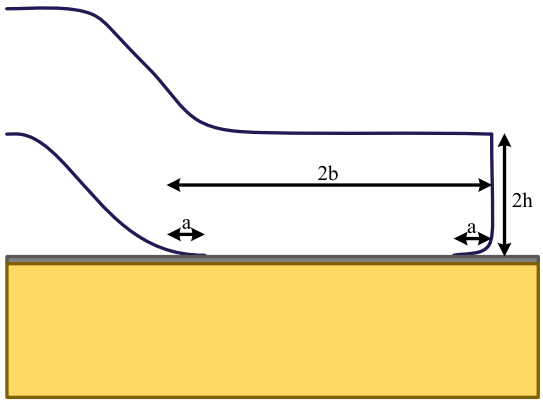

Fig. 6. Instruction of the geometry parameters used.

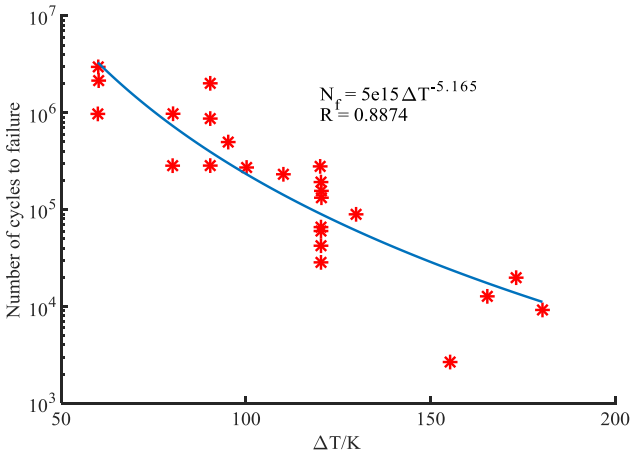

Fig. 7. Number of cycles to failure of metallization as a function of ΔT [45].

almost constant for different temperatures and the temperature effects to $v_{\mathrm{ce,on}}$ can be compensated as

$$v^{c}_{\mathrm{ce,on}} = v_{\mathrm{ce,on}} - \gamma\left(T - T_0\right) \tag{7}$$

where $v^{c}_{\mathrm{ce,on}}$ represents the compensated $v_{\mathrm{ce,on}}$, γ is the temperature coefficient, T indicates the corresponding temperature of the sampled $v_{ce,\mathrm{on}}$, and T_0 denotes the reference temperature.

2) Aluminum Metallization Reconstruction: The mismatching of the CTE produces stress to the aluminum, which is large enough to cause plastic deformation and forms the hillocks and cracks in the metallization. As a result, the sheet resistance rises and $v_{\mathrm{ce,on}}$ increases accordingly. The relationship between the number of cycles to failure and ΔT is given in Fig. 7, as obtained in [44]. The failure criterion is selected to be an 8% increase of $v_{\mathrm{ce,on}}$. Thus, the voltage shift of each cycle can be approximated by

$$\Delta v_{\mathrm{ce,on}} = k\frac{8\% \times v_{\mathrm{ce,on0}}}{5 \times 10^{15}\Delta T^{-5.165}} \tag{8}$$

where $v_{\mathrm{ce,on0}}$ is the initial value of $v_{\mathrm{ce,on}}$, and k is the constant that is to be identified. In fact, k is a variable at the early stage and approaches to a constant later [45]. Therefore, if (8) is utilized in the evolution model of $v_{\mathrm{ce,on}}$, it should wait until k reaches a stable state. Generally, the data from another device could lead to a nonnegligible error in the model. However, it could be acceptable here because the metallization is rather a general component without much difference between the different devices.

3) Bond Wire Liftoff: It was pointed out earlier that the voltage drop across the wire bonds with respect to the bond crack can be expressed as [30]

$$V_{\mathrm{WB}} = v_0 + \frac{\eta}{1 - \xi \cdot \mathrm{cycle}} \tag{9}$$

where V_{WB} is the wire-bonds voltage, v_0 is the initial voltage, and η and ξ are the model parameters.

However, two problems should be noted for this equation. First, it implies that the crack propagation rate keeps constant all the time regardless of the crack length and the temperature, which is contradictory to (6). The reason for this may be that it is based on the results in [46], which is under high temperature that could trigger the recovery mechanism called annealing, and then, changes the crack propagation rate. Yet such a high temperature is unlikely to happen in practice. On the other hand, the initial voltage of the wire bonds is difficult to know. Based on the aforementioned two reasons, a finite-element simulation is preferred here to link the crack length and the increased voltage together, with consideration of the uneven temperature distribution.

Fig. 8 shows the finite-element simulation results of the temperature ratio of each bond to the hottest bond 11 at different currents. It can be found that the ratios almost keep constant in spite of the load variation. This feature provides the possibility of simulating crack propagation under different loads. By substituting the stress–strain curve of Fig. 5(b) into (6), the crack propagation law can be obtained in (10) shown at bottom of this page.

Then, the ratio of each bond crack length to the crack length of the bond 11 is

$$\frac{\Delta a_i}{\Delta a_{11}} = \left(\left(\frac{\Delta T_i}{\Delta T_{11}}\right)^{0.4298} f(a_i, a_{11})\right)^{3.2} \tag{11}$$

where Δa_i represents the crack increase of each bond, Δa_{11} is crack increase of the bond 11, a_i is the crack length of each bond, and a_{11} is the crack length of the bond 11.

$$\frac{da}{dN} = C\left[7.54 \times \left(66.088(\Delta\alpha \cdot \Delta T \times 100\%)^{0.4298}\right) \cdot \sqrt{\pi \cdot a} \times \frac{1.122 - 0.56\,(a/b) - 0.205(a/b)^2 + 0.471(a/b)^3 - 0.190(a/b)^4}{\sqrt{1 - a/b}}\right]^{3.2} + \sigma_1 \tag{10}$$

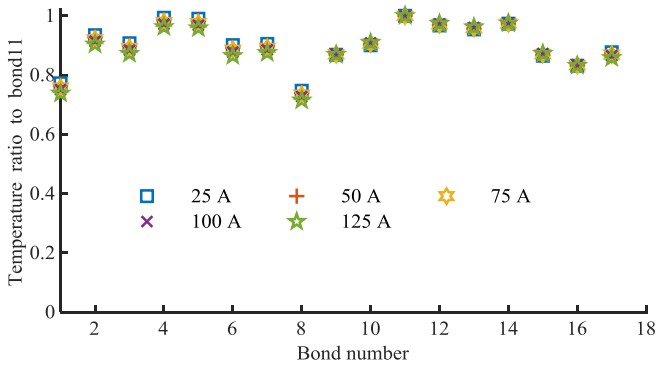

Fig. 8. Temperature ratio of each bond to bond 11 at different currents (bond 17 is the sensing point).

Thus, the crack propagation of each bond with respect to the crack length of the bond 11 can be simulated as Fig. 9(a). The temperature ratios of all the bonds to the bond 11 at the different crack ratios of the bond 11 are given in Fig. 9(b). It can be seen that the ratios are almost constant despite the crack length increasing, which demonstrates the effectiveness of the simulated crack length. Finally, the increased voltage with respect to the bond 11 crack length can be obtained through finite-element simulation according to the crack propagation, as shown in Fig. 9(c).

Overall, the output equation, i.e., the evolution of $v_{\mathrm{ce,on}}$ as a function of the crack ratio of the bond 11, can be obtained as given in (12) in millivolts (temperature compensated)

$$v^{c}_{\mathrm{ce,on}} = \underbrace{v_{\mathrm{ce,on0}}}_{\text{initial value}} + \underbrace{0.9091\left(\frac{a_{11}}{b}\right)^{2} + 3.0303\left(\frac{a_{11}}{b}\right) - 0.0327}_{\text{bond wire fatigue increase}} + \underbrace{\sum_{n=1}^{N} k\frac{8\% \times v_{\mathrm{ce,on0}}}{5 \times 10^{15}\Delta T_{11n}^{-5.165}}}_{\text{reconstruction increase}} + \sigma_2 \tag{12}$$

where ΔT_{11n} is the temperature swing of the bond 11 at step n, a_{11} can be calculated by (6), and σ_2 represents the measurement noise.

So far, the state-space model of the degradation process has been established, as given in (6) and (12).

C. Failure Criterion

Though a 5% increase of $v_{ce,\mathrm{on}}$ is widely adopted as the failure criterion of IGBTs in past works, another criterion is utilized in this article. It is based on the knowledge that once the first bond wire is lifted off, the current densities of the rest wires become higher and accelerate the degradation process. This positive feedback grows more and more severe until the IGBT fails in a relatively short time. Thus, it is reasonable to select the first bond wire liftoff as the failure criterion. In this article, once Δk reaches the fracture toughness K_c (14 MPa·m$^{1/2}$), which means the crack propagation enters the unstable region and the liftoff is considered to occur.

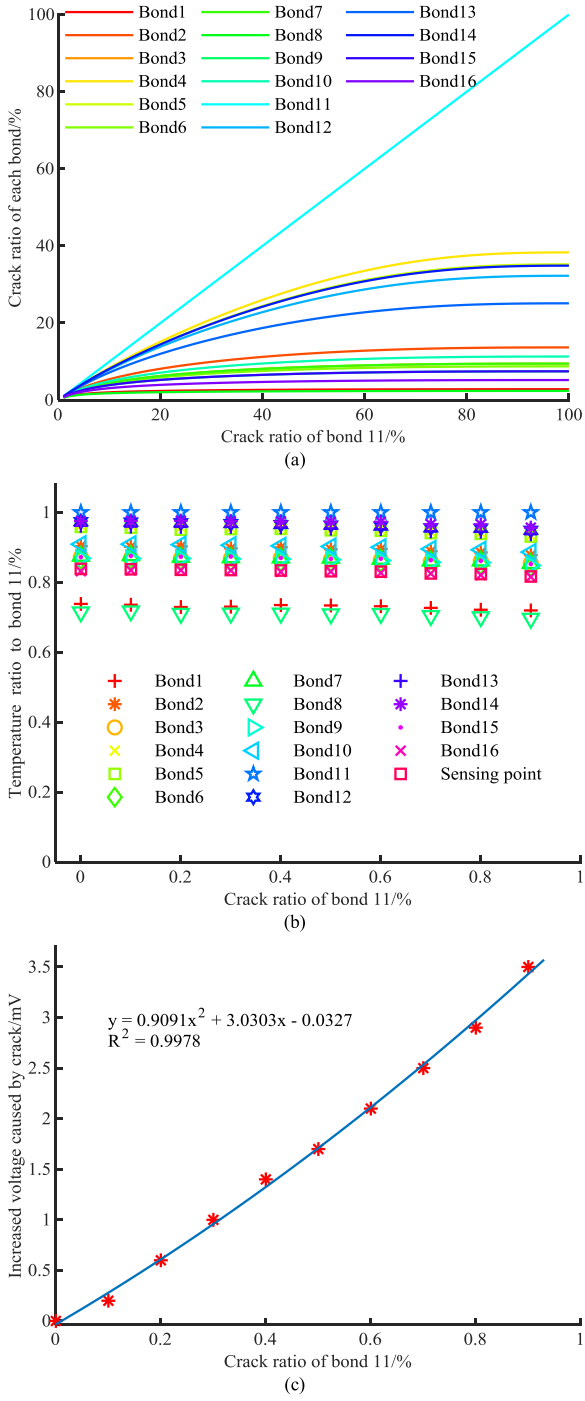

Fig. 9. (a) Crack evolution with respect to bond 11. (b) Temperature ratios of all the bonds to the bond 11 at different crack ratio of bond 11. (c) Increased voltage caused by the crack with respect to the bond 11 crack length.

IV. RUL Prediction

A. Parameter Learning Algorithm

Though the state-space model of the crack propagation has been built in Section III, the model parameters C, k, σ_1, and σ_2 of (6) and (12) are still unknown. They must be identified before predicting the RUL. Here, marginalized resample–move approach (MRMA) is adopted for parameter learning and state estimation, which is proposed by Andras and Junye [47]. It can

estimate the model parameter and the state sequentially when a new observation comes in, through the following three steps.

1) Augmentation Step: Denote all the random quantities of the particle filter in step l by u_l, the corresponding density is as given in (13), and the likelihood of the new observation is as written in (14)

$$\psi\left(u_{1:t}|\, y_{1:t}, \theta\right) = \prod_{l=2}^{t} \psi\left(u_l|\, u_{l-1}, y_l, \theta\right) \psi\left(u_1|\, y_1, \theta\right) \quad (13)$$

$$\hat{p}\left(y_t|\, y_{1:t-1}, \theta\right) \equiv \hat{p}\left(y_t|\, u_t, u_{t-1}, \theta\right) \quad (14)$$

where y represents the observation and θ is the parameter set.

Samples drawn from $\psi(u_t|u_{t-1}^{(n)},\ y_t,\ \theta^{(n)})$ can be obtained by running the particle filter on the new observation y_t for each θ, which can reduce the computation burden.

2) Reweighting Step: The incremental weights are calculated by using the (14). Thus, the updated weights can be given by

$$s_t^{(n)} = s_{t-1}^{(n)} \times \hat{p}\left(y_t|\, u_t^{(n)}, u_{t-1}^{(n)}, \theta^{(n)}\right). \quad (15)$$

Meanwhile, the likelihood of the parameters is given as

$$\hat{p}(y_{1:t}|\,\theta)^{(n)} = \hat{p}(y_{1:t-1}|\,\theta)^{(n)} \times \hat{p}\left(y_t|\, u_t^{(n)}, u_{t-1}^{(n)}, \theta^{(n)}\right). \quad (16)$$

Then, the target distribution can be approximated by the weighted sample $\{(\theta^{(n)}, u_t^{(n)}, \hat{p}(y_{1:t}|\theta)^{(n)}), s_t^{(n)}\}$.

3) Resample-Move Step: To maintain the effective particle size, the resample process will be executed once the effective particle size falls below the threshold B_1. Afterward, if the unique particles fall below the threshold B_2, each particle will be moved through a Markov kernel to enhance the diversity of the particles, without changing the original distribution. Please refer to [48] for more details of the algorithm.

B. State Estimation and RUL Prediction

After the parameters have been identified, the state of the crack length of the bond 11 at step t can be estimated by

$$a_{11,t} = \sum_{n=1}^{100} x_t^{(n)} \cdot w_t^{(n)} \quad (17)$$

where $x^{(n)}$ are the particles for the state and $w^{(n)}$ are the corresponding normalized weights; both are at step t.

The prediction method is similar to the conventional history-data-based approach. The particles produced by MRMA, which can approximate the posterior distribution of the crack length of the bond 11 will evolve step by step according to (10) until all of them reach the failure criteria. Note the predictions will not be corrected by the future $v_{\mathrm{ce,on}}$, which is unavailable at the prediction step. Then, substituting (4), (5), and (17) into (3), Δk at step t can be obtained. Consequently, the ending step that the Δk exceeds the K_c can be predicted and the RUL can be estimated. The flowchart of the prediction method is given in Fig. 10. Though the future junction temperatures are also unavailable, it could be estimated by the history mission profile for the repetitive load applications. Thus, the following prediction results of DUT#1 are based on the fact that the future temperature is known. The overall schematic of the prognostics is given in Fig. 11.

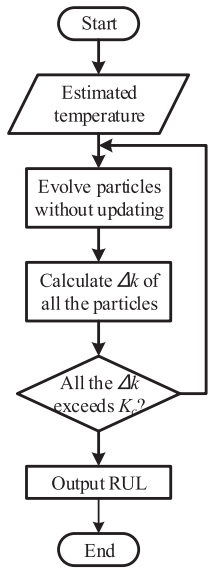

Fig. 10. Flowchart of the prediction method.

V. Experimental Results and Comparisons

A. Power Cycling Test

To collect the history data of $v_{\mathrm{ce,on}}$, and validate the proposed prognostic method, the accelerated power cycling test has been performed on a commercial IGBT module (FS150R12KT4 from Infineon). It is a six-pack trench field stop module capable of blocking 1200-V voltage and conducting 150-A current. The configuration of the test setup is shown in Fig. 1. The dc current source is utilized to provide the 125-A current to the two devices under test (DUTs). The DUTs are triggered by an FPGA alternately for 2 s with +15/−10-V gate voltage, through which they will be heated by the power loss and cooled by the cooling plate repeatedly. As a consequence, sizeable thermomechanical stress is applied to the DUTs, and the aging process is accelerated.

The overall system is depicted in Fig. 12. During the power cycling test, the maximum junction temperature, minimum junction temperature, and $v_{\mathrm{ce,on}}$ are recorded for each cycle. The junction temperature is approximated by the die surface temperature, which is measured by putting an optical filter on the die surface. As for $v_{\mathrm{ce,on}}$, it is measured by voltage probes of the oscilloscope. The test lasts for about 300 kilocycles until the gate–emitter short of DUT#1 (see Fig. 1) occurs. This could be attributed to the bond wire liftoff, which leads to the large current in remaining bond wires and forms a local hotspot around the left wire bonds on the chip [33].

The results are given in Fig. 13. The v_{ce1}, $T_{j\max 1}$, and $T_{j\min 1}$ represent the ON-state voltage, maximum junction temperature, and minimum junction temperature of the DUT#1, while v_{ce2}, $T_{j\max 2}$, and $T_{j\min 2}$ indicate the same parameters for the DUT#2. The initial T_j of DUT#1 is from 77.3 °C to 150.2 °C, with 72.9 °C temperature variation (ΔT). On the other hand, ΔT

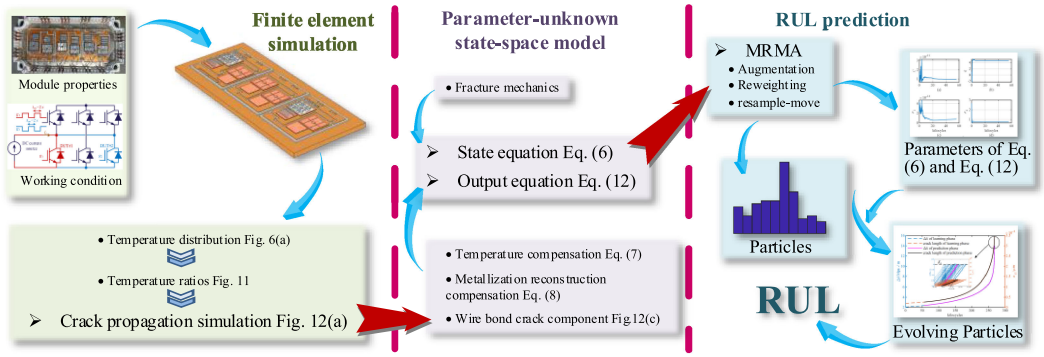

Fig. 11. Schematic of the proposed prognostic method.

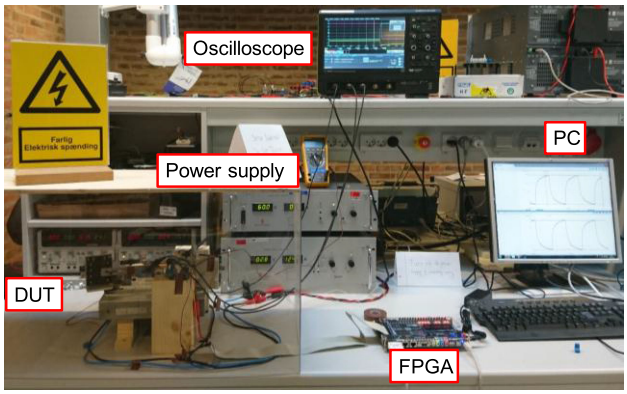

Fig. 12. Accelerated power cycling test set-up for six-pack IGBT module.

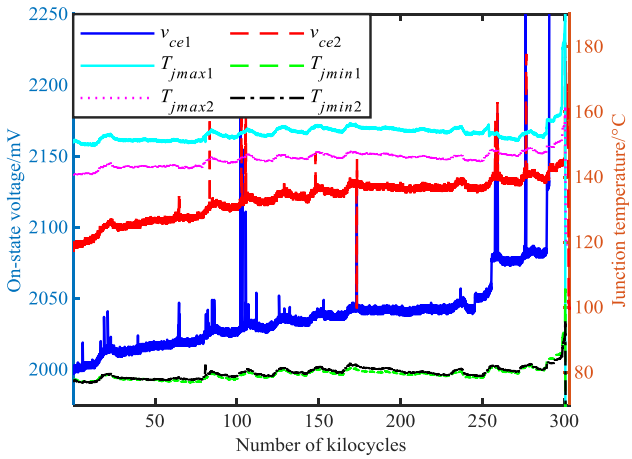

Fig. 13. Accelerated power cycling test results of the six-pack IGBT module.

of the DUT#2 is 63.4 °C, which varies from 77.2 °C to 140.6 °C. It explains the fact that the DUT#2 is still in good health state (no $v_{\mathrm{ce,on}}$ jump is found in DUT#2) when the DUT#1 has failed, as it suffers lower thermomechanical stress. All of the temperatures rise during the power cycling test due to the increase of both $v_{\mathrm{ce,on}}$ and thermal resistance of the DUT caused by degradation. The fluctuation of the temperature could be caused by daylight during the sunny days.

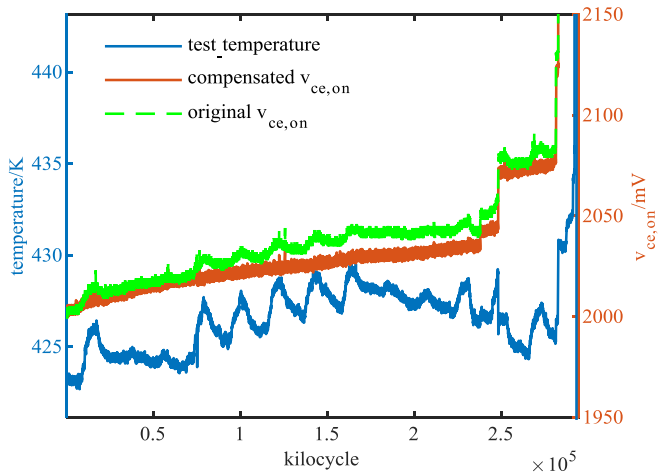

Fig. 14. Temperature compensation of DUT#1 $v_{\mathrm{ce,on}}$.

B. Temperature Compensation Results

By taking the first sampled maximum temperature as the reference, the compensated results of the DUT#1 $v_{\mathrm{ce,on}}$ evolution is shown in Fig. 14. It can be seen that both the temperature fluctuations caused by the daylight and the temperature drift caused by the increasing power loss can be compensated adequately. It should be noted that the initial phase, when $v_{\mathrm{ce,on}}$ increases, while the temperature goes down, has been disregarded. This phenomenon could be attributed to the adjustment of the thermal interface material (TIM). Meanwhile, the measurement spikes are filtered out for better prediction performance.

C. Parameter Learning Results

The initial guess of the unidentified parameters is given as

$$\theta_0 = \{C_0, k_0, \sigma_1, \sigma_2\} = \{5 \times 10^{-12}, 1, 5 \times 10^{-14}, 3\}. \quad (18)$$

The particle size is set as 100×100 for the parameters and state. The thresholds of B_1 and B_2 are 50 and 50, respectively.

The learning phase stops when all the parameters approach the stable state. In the case of DUT#1, it is about 56 kilocycles, and the estimated values of the parameters are as shown in Fig. 15, which are $\{9.59 \times 10^{-12}, 4.67, 7.80 \times 10^{-15}, 0.76\}$.

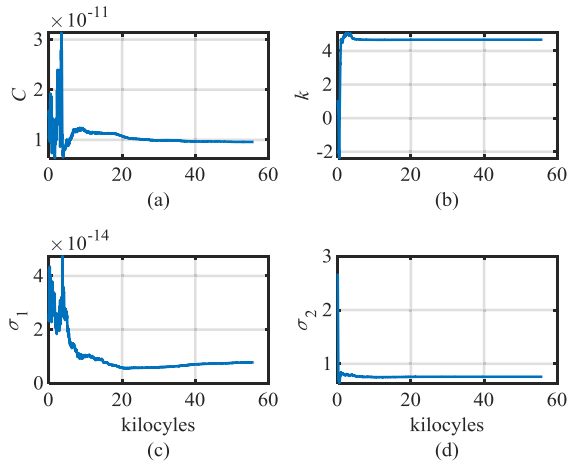

Fig. 15. State-space model parameters learned by MRMA.

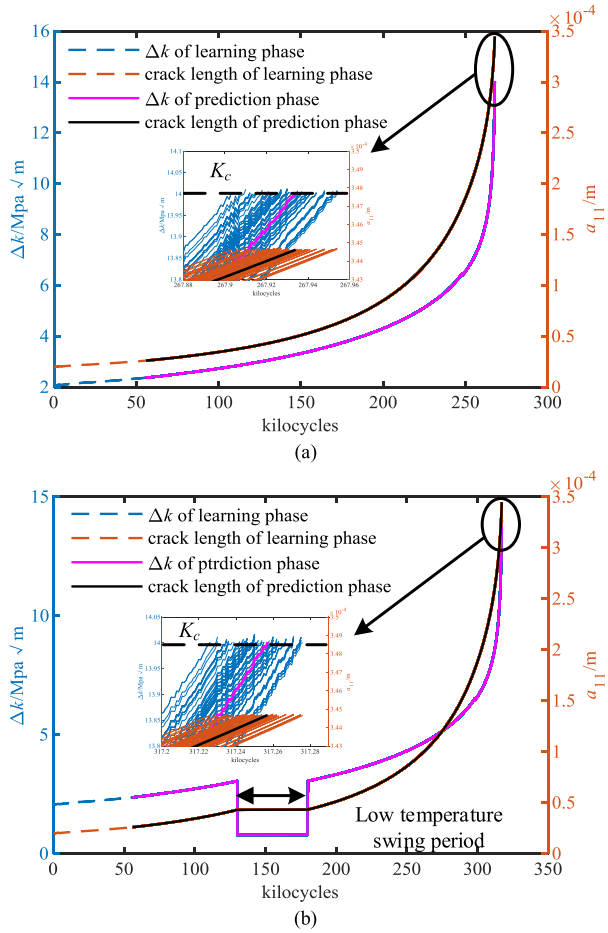

Fig. 16. Prediction results when (a) future temperature can be estimated, and (b) future temperature can be estimated and includes low-temperature swing.

D. RUL Prediction Results

The temperature measured during the power cycling test is used directly to represent the estimation of the temperature. The results are shown in Fig. 16(a). The IGBT is predicted to fail at 268 kilocycle when the Δk exceeds the K_c, while the actual failure time is 238 kilocycle, indicating the prediction error is 12.61%. To validate the effectiveness of the temperature swing sensitivity, a period of 50 kilocycles with $\Delta T = 5$ °C is inserted at 130 kilocycle. Given the fact that the IGBT degrades so slow under such small ΔT, the actual lifetime is considered as 288 kilocycles. The prediction results are shown in Fig. 16(b), which is 317 kilocycles, with the prediction error of 10.07%. It could also be seen from the plateaus of both the crack length and Δk that the extrapolation methods are not applicable in this case, neither from the curve-fitting perspective nor the fracture mechanics approach.

TABLE III
COMPARISON OF N_{pc}

Methods	C-M*	A-C-M*	Method in [23]	Proposed method
N_{pc}	2	3	7	0

*C-M: Coffin–Manson model; A-C-M: Arrhenius–Coffin–Manson model

TABLE IV
COMPARISON OF PREDICTION ERROR

Condition	Prediction error/e_p			
	Curve fitting	PF	APF	Proposed method
w/o TSV	20.71%	-10.14%	-9.29%	12.61%
w/ TSV	2.42%	-23.76%	-23.03	10.07%
Δe_p^*	18.29%	13.62%	13.74%	2.54%

*: Δe_p = difference of prediction errors w/ and w/o TSV.

E. Comparison With Conventional Methods

1) Comparison With Model-Driven Methods: To show the cost effectiveness, the comparison between the proposed method and the conventional data-driven methods is given in Table III in terms of the minimum number of required power cycling tests N_{pc}. It can be seen that the conventional methods require 2–7 N_{pc}, while the proposed method requires no power cycling tests for parameter tuning (the power cycling test presented in this section is for validation). It should be pointed out that N_{pc} is the minimum number that ensures the parameters can be calculated. More tests will be required if an accurate lifetime model is desired. In this sense, the proposed method is more cost effective than the conventional model-driven methods.

2) Comparison With Data-Driven Methods: To show the capability of dealing with varied temperature swings, the comparison between the proposed method and the curve fitting/filter-based data-driven methods is given in Table IV. It must be pointed out that the curve fitting/filter-based data-driven methods are based on $v_{\mathrm{ce,on}}$ and the failure criterion is 5% increase of $v_{\mathrm{ce,on}}$, which results in the lifetime equaling 280k cycles without TSV and 330 kilocycles with TSV. The curve-fitting equation is based on (9) and the fitted equation is given in (19). Its prediction results with and without temperature swing variation are both 338 kilocycles because it is not able to use the temperature information. As a result, the prediction errors (e_p) are 20.71% and 2.42% for the different conditions. Note that it is just a coincidence that e_p of the condition with TSV is so low. If the duration of the low-temperature swing is set as 150 kilocycles,

the prediction error would be large (–21.4%)

$$v_{\mathrm{ce,on}} = 2002 + 0.00029 \times \mathrm{cycle} + \frac{0.1654}{1 - 0.6652 \times \mathrm{cycle}}. \tag{19}$$

The equation used for PF and APF are the same as [31], and the fitted model is given as follows:

$$v_{\mathrm{ce,on},n} = v_{\mathrm{ce,on},n-1} + 2 \times 2.164 \times 10^{-12} \times \mathrm{cycle} + 0.000396. \tag{20}$$

The prediction results of PF and APF for both conditions are 251.6 kilocycle and 254 kilocycles, respectively.

It can be seen from Table IV that the prediction errors of all the three conventional methods are of huge difference under different conditions, while the proposed method has a robust performance, which shows its advantage of dealing with TSV condition.

VI. Conclusion

A cost-effective prognostic method for the IGBT bond wire that considers the temperature swing has been presented in this article. The conclusions can be drawn as follows.

1) $v_{\mathrm{ce,on}}$ could be a good indicator for predicting the RUL. Nevertheless, the irrelevant component, e.g., the voltage shift caused by the temperature variation or other degradation mechanisms, must be compensated before prediction.
2) The relationship between the increase of $v_{\mathrm{ce,on}}$ and the degradation state of the bond wire can be revealed by the finite-element simulation.
3) The temperature ratio of each bond to the hottest bond is almost kept constant under different load currents and degradation states.
4) The system model is established from the fracture mechanism theory. Compared to the conventional model-based methods, it does not require a large number of power cycling tests, which can reduce the temporal and economic costs.
5) The particle-based MRMA can estimate the unknown parameters of the system model.
6) The proposed method can predict the RUL under temperature swing variation if the temperature information can be obtained, with a prediction error of about 10%. The error could be introduced from the curve fittings, temperature compensation or system modeling, parameter learning algorithm, and disregard of the initial phase.

It should be pointed out that the temperature is measured by the optical fibers, which are unlikely to be used in practice. In this case, temperature-sensitive electrical parameters that are not affected by degradation could be a solution.

References

[1] V. Yaramasu, B. Wu, P. C. Sen, S. Kouro, and M. Narimani, "High-power wind energy conversion systems: State-of-the-art and emerging technologies," *Proc. IEEE*, vol. 103, no. 5, pp. 740–788, May 2015.

[2] L. Dorn-Gomba, P. Magne, B. Danen, and A. Emadi, "On the concept of the multi-source inverter for hybrid electric vehicle powertrains," *IEEE Trans. Power Electron.*, vol. 33, no. 9, pp. 7376–7386, Sep. 2018.

[3] T. Kim and S. Kwak, "A flexible voltage bus converter for the 48-/12-V dual supply system in electrified vehicles," *IEEE Trans. Veh. Technol.*, vol. 66, no. 3, pp. 2010–2018, Mar. 2017.

[4] H. Chen, H. Kim, R. Erickson, and D. Maksimovic, "Electrified automotive powertrain architecture using composite DC-DC converters," *IEEE Trans. Power Electron.*, vol. 32, no. 1, pp. 98–116, Jan. 2017.

[5] D. L. H. Aik and G. Andersson, "Fundamental analysis of voltage and power stability of single-infeed voltage-source converter HVDC systems," *IEEE Trans. Power Del.*, vol. 34, no. 1, pp. 365–375, Feb. 2019.

[6] S. P. Engel, M. Stieneker, N. Soltau, S. Rabiee, H. Stagge, and R. W. D. Doncker, "Comparison of the modular multilevel DC converter and the dual-active bridge converter for power conversion in HVDC and MVDC grids," *IEEE Trans. Power Electron.*, vol. 30, no. 1, pp. 124–137, Jan. 2015.

[7] B. Gou, "Fault diagnosis and fault-tolerant control technology of railway electrical traction converter," Ph.D. dissertation, Dept. Elect. Eng., Southwest Jiaotong Univ., Chengdu, China, 2016.

[8] L. M. Moore and H. N. Post, "Five years of operating experience at a large, utility-scale photovoltaic generating plant," *Prog. Photovolt., Res. Appl.*, vol. 16, no. 3, pp. 249–259, 2008.

[9] S. Yang, A. Bryant, P. Mawby, D. Xiang, L. Ran, and P. Tavner, "An industry-based survey of reliability in power electronic converters," *IEEE Trans. Ind. Appl.*, vol. 47, no. 3, pp. 1441–1451, May/Jun. 2011.

[10] H. Wang *et al.*, "Transitioning to physics-of-failure as a reliability driver in power electronics," *IEEE J. Emerg. Sel. Topics Power Electron.*, vol. 2, no. 1, pp. 97–114, Mar. 2014.

[11] H. Wang, M. Liserre, and F. Blaabjerg, "Toward reliable power electronics: challenges, design tools, and opportunities," *IEEE Ind. Electron. Mag.*, vol. 7, no. 2, pp. 17–26, Jun. 2013.

[12] H. Oh, B. Han, P. McCluskey, C. Han, and B. D. Youn, "Physics-of-failure, condition monitoring, and prognostics of insulated gate bipolar transistor modules: A review," *IEEE Trans. Power Electron.*, vol. 30, no. 5, pp. 2413–2426, May 2015.

[13] C. Busca *et al.*, "An overview of the reliability prediction related aspects of high power IGBTs in wind power applications," *Microelectron. Rel.*, vol. 51, no. 9–11, pp. 1903–1907, 2011.

[14] X. Fang, S. Lin, X. Huang, F. Lin, Z. Yang, and S. Igarashi, "A review of data-driven prognostic for IGBT remaining useful life," *Chin. J. Elect. Eng.*, vol. 4, no. 3, pp. 73–79, 2018.

[15] U.-M. Choi and F. Blaabjerg, "Separation of wear-out failure modes of IGBT modules in grid-connected inverter systems," *IEEE Trans. Power Electron.*, vol. 33, no. 7, pp. 6217–6223, Jul. 2018.

[16] M. Ahsan, S. Stoyanov, and C. Bailey, "Data driven prognostics for predicting remaining useful life of IGBT," in *Proc. 39th Int. Spring Semin. Electron. Technol.*, Pilsen, Czech Republic, May 18–22, 2016, pp. 273–278.

[17] H. Huang and P. A. Mawby, "A lifetime estimation technique for voltage source inverters," *IEEE Trans. Power Electron.*, vol. 28, no. 8, pp. 4113–4119, Aug. 2013.

[18] P. D. Reigosa, H. Wang, Y. Yang, and F. Blaabjerg, "Prediction of bond wire fatigue of IGBTs in a PV inverter under a long-term operation," *IEEE Trans. Power Electron.*, vol. 31, no. 10, pp. 7171–7182, Oct. 2016.

[19] L. R. GopiReddy, L. M. Tolbert, B. Ozpineci, and J. O. P. Pinto, "Rainflow algorithm-based lifetime estimation of power semiconductors in utility applications," *IEEE Trans. Ind. Appl.*, vol. 51, no. 4, pp. 3368–3375, Jul./Aug. 2015.

[20] M. Musallam, C. Yin, C. Bailey, and M. Johnson, "Mission profile-based reliability design and real-time life consumption estimation in power electronics," *IEEE Trans. Power Electron.*, vol. 30, no. 5, pp. 2601–2613, May 2015.

[21] M. Held, P. Jacob, G. Nicoletti, P. Scacco, and M.-H. Poech, "Fast power cycling test for IGBT modules in traction application," in *Proc. 2nd Int. Conf. Power Electron. Drive Syst.*, Singapore, May 26–29, 1997, pp. 425–430.

[22] A. Syed, "Limitations of Norris-Landzberg equation and application of damage accumulation based methodology for estimating acceleration factors for Pb free solders," in *Proc. 11th Int. Thermal, Mech. Multi-Phys. Simul. Exp. Microelectron. Microsyst.*, Bordeaux, France, Apr. 26–28, 2010, pp. 1–11.

[23] R. Bayerer, T. Herrmann, T. Licht, J. Lutz, and M. Feller, "Model for power cycling lifetime of IGBT modules—Various factors influencing lifetime," in *Proc. 5th Int. Conf. Integr. Power Electron. Syst.*, Nuremberg, Germany, Mar. 18–22, 2008, pp. 1–6.

[24] N. Dornic *et al.*, "Stress-based model for lifetime estimation of bond-wire contacts using power cycling tests and finite element modelling," *IEEE J. Emerg. Sel. Topics Power Electron.*, vol. 7, no. 3, pp. 1659–1667, Sep. 2019.

[25] H. Berg and E. Wolfgang, "Advanced IGBT modules for railway traction applications—Reliability testing," *Microelectron. Rel.*, vol. 38, pp. 1319–1323, 1998.
[26] V. Smet *et al.*, "Ageing and failure modes of IGBT modules in high-temperature power cycling," *IEEE Trans. Ind. Electron.*, vol. 58, no. 10, pp. 4931–4941, Oct. 2011.
[27] A. Alghassi, S. Perinpanayagam, and M. Samie, "Stochastic RUL calculation enhanced with TDNN-based IGBT failure modeling," *IEEE Trans. Rel.*, vol. 65, no. 2, pp. 558–573, Jun. 2016.
[28] A. Alghassi, S. Perinpanayagam, M. Samie, and T. Sreenuch, "Computationally efficient, real-time, and embeddable prognostic techniques for power electronics," *IEEE Trans. Power Electron.*, vol. 30, no. 5, pp. 2623–2634, May 2015.
[29] M. Samie, A. Alghassi, and S. Perinpanayagam, "Unified IGBT prognostic using natural computation," in *Proc. IEEE Int. Conf. Dig. Signal Process.*, Singapore, Jul. 21–24, 2015, pp. 698–702.
[30] N. Degrenne and S. Mollov, "Experimentally-validated models of on-state voltage for remaining useful life estimation and design for reliability of power modules," in *Proc. 10th Int. Conf. Integr.Power Electron. Syst.*, Stuttgart, Germany, Mar. 20–22, 2018, pp. 1–6.
[31] N. Patil, D. Das, and M. Pecht, "A prognostic approach for non-punch through and field stop IGBTs," *Microelectron. Rel.*, vol. 52, no. 3, pp. 482–488, 2012.
[32] M. S. Haque, S. Choi, and J. Baek, "Auxiliary particle filtering-based estimation of remaining useful life of IGBT," *IEEE Trans. Ind. Electron.*, vol. 65, no. 3, pp. 2693–2703, Mar. 2018.
[33] M. Akbari, A. S. Bahman, P. D. Reigosa, F. Iannuzzo, and M. T. Bina, "Thermal modeling of wire-bonded power modules considering non-uniform temperature and electric current interactions," *Microelectron. Rel.*, vol. 88–90, pp. 1135–1140, 2018.
[34] R. Wu *et al.*, "A temperature-dependent thermal model of IGBT modules suitable for circuit-level simulations," *IEEE Trans. Ind. Appl.*, vol. 52, no. 4, pp. 3306–3314, Jul./Aug. 2016.
[35] W.-S. Loh, M. Corfield, H. Lu, S. Hogg, T. Tilford, and C. M. Johnson, "Wire bond reliability for power electronic modules—Effect of bonding temperature," in *Proc. Int. Conf. Thermal, Mech. Multi-Phys. Simul. Experiments Microelectronics Micro-Syst.*, London, U.K., Apr. 16–18, 2007, pp. 1–6.
[36] E. Arjmand, P. A. Agyakwa, M. R. Corfield, J. Li, B. Mouawad, and C. Mark Johnson, "A thermal cycling reliability study of ultrasonically bonded copper wires," *Microelectron. Rel.*, vol. 59, pp. 126–133, 2016.
[37] R. Ruffilli, "Fatigue mechanisms in Al-based metallizations in power MOSFETs," Ph.D. dissertation, École doctorale Sciences de la Matière, Université Paul Sabatier, Toulouse, France, 2017.
[38] F. Z. Ralf Schmidt, "Impact of absolute junction temperature on power cycling lifetime," in *Proc. 15th Eur. Conf. Power Electron. Appl./ECCE Eur.*, Lille, France, Sep. 2–6, 2013, pp. 1–10.
[39] P. Paris and F. Erdogan, "A critical analysis of crack propagation laws," *J. Basic Eng.*, vol. 84, no. 4, pp. 28–533, 1963.
[40] G. Khatibi, M. Lederer, B. Weiss, T. Licht, J. Bernardi, and H. Danninger, "Accelerated mechanical fatigue testing and lifetime of interconnects in microelectronics," *Procedia Eng.*, vol. 2, no. 1, pp. 511–519, 2010.
[41] H. Tada, P. C. Paris, and G. R. Irwin, *The Stress Analysis of Cracks Handbook*, 3rd ed. New York, NY, USA: ASME Press, 2000.
[42] N. R. Mohsin, "Comparison between theoretical and numerical solutions for center, single edge and double edge cracked finite plate subjected to tension stress," *Int. J. Mech. Prod. Eng. Res. Develop.*, vol. 5, no. 2, pp. 11–20, 2015.
[43] Y. Lu and A. Christou, "Prognostics of IGBT modules based on the approach of particle filtering," *Microelectron. Rel.*, vol. 92, pp. 96–105, 2019.
[44] C. Durand, M. Klingler, D. Coutellier, and H. Naceur, "Failure mechanisms and reliability of the Al-chipmetallization during power cycling," in *Proc. 22ème Congrès Français de Mécanique*, Lyon, France, Aug. 24–28, 2015, pp. 1–19.
[45] M. Brincker, K. B. Pedersen, P. K. Kristensen, and V. Popok, "Passive thermal cycling of power diodes under controlled atmospheric conditions—Effects on metallization degradation," in *Proc. 9th Int. Conf. Integr. Power Electron. Syst.*, Nuremberg, Germany, Mar. 8–10, 2016, pp. 1–6.
[46] Y. Yamada *et al.*, "Reliability of wire-bonding and solder joint for high temperature operation of power semiconductor device," *Microelectron. Rel.*, vol. 47, no. 12, pp. 2147–2151, 2007.
[47] A. Fulop and J. Li, "Efficient learning via simulation: A marginalized resample-move approach," *J. Econometrics*, vol. 176, no. 2, pp. 146–161, 2013.
[48] S. Hartmann and E. Özkol, "Bond wire life time model based on temperature dependent yield strength," in *Proc. Int. Conf. Power Electron., Intell. Motion, Power Quality Energy Manage.–Europe.*, Nuremberg, Germany, May 8–10, 2012, pp. 494–501.